

Performance Evaluation of Internal Combustion Engine Under Noise Measurements an Experimental and Analytical Procedure

P. Korkos^a, P.G. Nikolakopoulos^{a,*}

^aMachine Design Laboratory, Department of Mechanical and Aeronautics Engineering, University of Patras, 26500, Greece.

Keywords:

Piston ring tribology
Noise measurements
Wavelets
Piston slap

* Corresponding author:

Pantelis G. Nikolakopoulos 
E-mail: pnikolakop@upatras.gr

Received: 30 August 2019

Revised: 12 October 2019

Accepted: 29 November 2019

ABSTRACT

Nowadays, the technology of internal combustion engines plays an important role, towards the energy consumption, since it is estimated that one third of the consumed fuel is aimed to counterbalance the friction. Special contribution at this issue has the piston ring – liner system and therefore, the finding of friction and minimum lubricant thickness are studied in order to evaluate its performance, in terms of energy consumption, due to friction and the emitted noise. The numerical methodology using computational fluid dynamics (CFD), solving the Navier-Stokes equations, is extended in order to predict the sound pressure level (SPL) of piston movement. Simultaneously, the contribution of the sound pressure level of crankshaft bearings is examined. The results are matched with experimental measurements of SPL which held at a single cylinder of 4 stroke gasoline Internal Combustion Engine. They were received at Top Dead Center and at the relevant crankshaft positions, both at thrust and antithrust side and useful conclusions are taken out. Then, the measurements were processed, using the method of wavelets in order to detect the rapid and impulsive phenomenon of piston slap. The most important piston slap events are shown, accordingly to their contribution at total power losses and their spectral content.

© 2020 Published by Faculty of Engineering

1. INTRODUCTION

The internal combustion engine is powers source of many widely used applications such us, in naval, and automotive industry and in many other industrial activities. The development of internal combustion engine in terms of heavy loads, high speeds, and light direction, its vibration and noise problems are

becoming increasingly serious and has become the main noise source component of naval and automotive applications due to its vibrations. By reducing the level of vibration and noise of the internal combustion engine, the working performance of the internal combustion engine can be improved, and the people's living environment can be also improved in higher quality standards [1]. In order to deal with the

vibration and noise reduction of the internal combustion engine, the first action is to accurately separate and identify the noise sources of the internal combustion engine.

Many parts of the internal combustion engine can produce worth note noise. According to the noise source of the internal combustion engine, the noise can be divided into mechanical noise, combustion noise, and aerodynamic noise in [2–3]. Mechanical noise mainly consists of piston slap noise, air valve knocking noise, gear meshing noise, and fuel injection pump noise. Combustion noise is due to change of the cylinder pressure. Aerodynamic noise includes intake noise, exhaust noise, and fan noise.

There are many investigators who have been utilized methods to separate and identify the noise sources of the internal combustion engine. The cyclic Wiener filtering method is described by Badaoui et al. [4], while the blind source separation method was presented in [5–7]. In addition the improved spectrofilter method was used by Pruvost et al. [8] and speed-varying filter was designed by Antoni et al. [9] to achieve this separation. Zhang et al. [10] adopted the ensemble empirical mode decomposition, to separate and identify the noise sources of the diesel engine. Bi et al. [11] utilised the EEMD-RobustICA method to separate the combustion noise, piston slap noise, and exhaust noise of the gasoline engine.

More often, a well-targeted improvement of the sound characteristics has been replaced by a simple reduction of the noise level. For several car manufacturers, especially those located in the premium segment, the so-called sound-design, has become an essential opportunity for defining and emphasizing brand image and vehicle characteristics. Seifriedsberger and Rumplmayr, in their article deal with the investigation of the combustion noise of passenger car diesel engines, which, especially in part load conditions, is clearly perceptible for passengers and passers [12].

Traditionally, noise signals are mainly analyzed with spectral analysis, i.e., the Fourier transform. However, the Fourier transform is not a proper tool for the analysis of internal combustion engine vibration and noise signals, as they are nonstationary and consist of many transient components. In recent years, a new signal

processing technique especially suitable for the nonstationary signal analysis in the time-frequency domain has been developed by Cohen et al. [13–14].

In the recent literature, there are many qualified works dealing with engine noise as well techniques and methods to analyze and to understand the phenomena produced by the engine's operation. An analytical and numerical approach is presented by Dolatabadi et al. in [15] for the calculation of the radiated noise due to internal combustion engine piston impacts on the cylinder liner through a film of lubricant. Quasi-static and transient dynamic analyses coupled with impact elasto-hydrodynamics have been reported. Continuous wavelet (CWT) signal processing is performed to identify the occurrence of piston slap noise events and their spectral content. They found good conformance between the predictions and experimentally acquired signals.

A coupled simulation of piston dynamics and engine tribology called tribodynamics has been performed by Dolatabadi et al. [16] using quasi-static and transient numerical codes. The inertia and the reaction forces developed in the piston have been also calculated. Their results show a good repeatability throughout the set of measurements which were obtained in terms of the number of events occurring and their locations during the engine cycle.

An analytical model is presented by Ohta et al. [17], regarding the impact force and the vibratory response of cylinder liner induced by the piston slap in internal combustion engines. The equation of motion for the coupled system of piston and cylinder liner is derived, taking account of several resonant modes of the cylinder liner to simulate accurately time histories of the impact force and the vibratory response. An example, of the piston slap phenomenon in a six cylinder diesel engine with wet liners is analyzed at rotational speeds of $N = 1800, 2300$ rpm.

Nakashima et al. [18] investigated the mechanism of the piston slap with a precisely numerical simulation. Simultaneous noise reduction in the conditions of both idling and high speed was achieved successfully by optimizing the piston's center of gravity as well as piston pin offset.

A new method, comprising Navier–Stokes equations, Rayleigh–Plesset volume fraction equation, an analytical control-volume thermal-mixed approach and asperity interactions, was presented by Shahmohamadi et al. [19]. Their method deals with the prediction of lubricant flow and assessment of friction in the compression ring–cylinder liner conjunction.

A detailed analysis is provided by Mishra et al. [20] of the compression ring-bore/liner conjunction. The authors in their analysis included ring-bore conformability and global in-plane deformation of ring fitted in situ, as well as the lubricated conjunction under a transient regime of lubrication, taking into account combined elastohydrodynamics and asperity interactions.

Liu and Randal [21] managed to separate the vibration sources due to piston slap, by using blind source separation techniques.

In the publication of Zavos and Nikolakopoulos [28], it was found that the elastodynamics thin ring performance showed thinner lubricant films and higher friction values when hot engine conditions were expected. In addition the developed methodology of CFD code solving Navier-Stokes equations is clearly stated in the relative publication by the same authors [33].

Mahdisoozani et al. [34] presented a study that aims to gather all the recent works, deal with the internal combustion engines conducted to reduce and isolate engine vibration, before transmitting to other vehicle parts such as drive shafts and chassis.

Rahmaniane et al. [35] developed a computational model which was used to study NO_x reduction during pulverized coal combustion. The finite volume method with a structured grid arrangement and a SIMPLE algorithm were utilized to model the pulverized coal combustion process. The effect of dilution of the oxidizer by participating gases including Air, Helium, Argon, Steam and CO₂ were studied, while the corresponding reductions in the rate of NO_x production have been compared.

Sadeghinezhada et al. [36] presented a review study referred in the comparison of the behavior between bio-fuels with conventional fuels for use in the internal combustion engines. One of

the main conclusions of their work was that, in the hot and cold environment bio-fuels was not fully convenient to replace the fossil fuels. However, in the controlled environment with modified combustion equipment bio-fuel can be used as an alternate fuel. An other one main conclusion, was that the researchers have seen that absolute utilization of bio-fuel is not appreciable as it will affect the food chain but the blend of bio-fuel with conventional fuel could precisely reduce its use and become beneficial to green house effect.

In the knowledge of authors there is not any work evaluating the engine performance at the same time taking measurements from both the crankshaft and compression piston ring. In this paper, an analytical model and experimental procedure were developed and presented. The combined noise measurements, processed with wavelets transformation, in piston ring and the crankshaft areas leads to a prediction of the sound pressure level SPL which is affected by the viscosity and asperities friction and consequently by piston slap having the computed power of energy losses and leads also to the determination of the piston slap events from the measurements. The total radiated noise is also studied.

The prediction of the pressures and friction forces on a parabolic profile of the upper compression ring using a 2D CFD validated model, matched with experimental measurements of sound pressure level are of the most significant highlights of this work.

The paper is organized as follows: in sections 1 and 2 the theoretical aspects of the wavelets and the flow equations are presented, while in section 3 the numerical model is analyzed. In section 4 the experimental procedure is shown and further in section 5 the results both analytical and experimental, are presented and discussed, while in section 6 the major findings are also presented.

2. THEORY

2.1 Signal processing (wavelets)

Some theory aspects concerning the wavelet transform are presented below [40]. Comparing

with Fast Fourier Transform (or Discrete Fourier Transform), wavelet is able to analyse data at the combined domain of frequency and time. Such type of analysis is suitable for signals that are characterized as non-periodic, includes transient events and also for stationary and non-stationary signals, and thus demonstrates some signal characteristics that can be analytically studied.

Wavelet transformation uses wave-like functions, which are the wavelets. Two types of wavelet transformation are distinguished: Discrete Transform (DWT) and Continuous Transform (CWT). For their implementation there are families of mother wavelets that have the ability to shift (along the axis of time) and expand or compress to make the information in the signal more distinct. It, therefore, includes two parameters: the scale and the shift.

The difference between Fourier and wavelet transformations is that, in the first one analysis, the signal as a superposition of harmonic and usually sinusoidal waves, is extended as infinity and are predictable. On the other hand, in the wavelet transformation, the signal is analysed using mother waves whose configuration is not as smooth as in the harmonics. In other words, in the continuous Fourier transform the signal is analysed in an infinite number of sinusoidal functions with a different coefficient each one. The result of the transformation is the Fourier coefficients, which when multiplied by a sinus of the appropriate frequency and summed, give the original signal. Correspondingly, continuous wavelet transformation transforms the signal to a sum of scaled and shifted wavelet functions ψ and the transformation result is scale and position related coefficients.

The scale of the transformation is related to the frequency for which the low scale corresponds to high frequencies and is ideal for rapidly changing events (compressed wave) and the high scale is the inverse of the low (stretched wavelet).

Wavelet transformation implemented by depicting the coefficients both in terms of time and frequency, have the potential to display more clearly at the time of a discontinuity and even identify its frequency content. They can also show trends, breakdown points, discontinuities to large derivatives, self-

similarity and can still be used to compress or de-noise a signal.

2.2 Wavelets Theory

The basic wavelet theory is presented in the below paragraphs [40].

The expression $\psi(t)$ is defined as follows including the parameters a and b , which represent respectively the scale and position of $\psi(t)$:

$$\psi_{a,b}(t) = \frac{1}{\sqrt{a}} \psi\left(\frac{t-b}{a}\right) \quad (1)$$

Furthermore, the Continuous Wavelet Transform (CWT) is calculated as:

$$T(a,b) = \frac{1}{\sqrt{a}} \int_{-\infty}^{+\infty} x(t) \psi^*\left(\frac{t-b}{a}\right) dt \quad (2)$$

There are many wavelets that can be used, which are very simple or might be also more complex. Also there is a possibility to create new ones. Some of them are Haar, Daubechies, Mexican hat, Gauss, Meyer, Morlet etc. The Morlet wavelet is very essential because it has the ability to display both the measure and the transformation phase and thus provides useful information. It also has the capability of detecting striking parts of the signal since the usual symptoms of errors in engineering devices are impulse signals. The Morlet wavelet is defined as:

$$\psi\left(\frac{t-b}{a}\right) = \frac{1}{\pi^{1/4}} e^{i2\pi f_0 \left[\frac{t-b}{a}\right]} e^{-\frac{1}{2}\left[\frac{t-b}{a}\right]^2} \quad (3)$$

It is very important to emphasize that CWT can be used at discrete time and consequently to process measurements taken at a specific time period. The main difference with the DWT is that the CWT can be used for any scale up to a maximum range defined by the signal analyst, taking into account its accuracy and computational power. CWT is also continuous in the shifting process, meaning that during the calculation the wave is smoothly shifted along the length of the signal. Finally, with regard to applications, it is preferred to use CWT when long time-precision analysis is desired across all scales.

The energy contained in a wavelet for a certain scale a and b is given by the two-dimensional wave energy density function as follows:

$$E(a,b) = |T(a,b)|^2 \quad (4)$$

The plot of $E(a,b)$ is a scalogram.

The methodical approach used in this work can be divided in two parts. The first one, concerning the investigations, realized on a single cylinder engine test bench using noise measurement techniques and the second, is regarding to the carried out simulations.

3. THE FLOW PROBLEM

3.1 Navier Stokes

In order to obtain the characteristic quantities of the fluid field, Navier-Stokes equations or momentum equations, as are alternatively called, coupled with the continuity equations should be solved. The continuity and Navier-Stokes equations are presented at the following relationships,

$$\frac{D\rho}{Dt} + \rho \nabla \vec{V} = 0 \quad (5)$$

$$\rho \frac{D\vec{V}}{Dt} = -\nabla \vec{p} + \nabla \cdot (\vec{\tau}) + \vec{F} \quad (6)$$

where ρ is the lubricant density, \vec{V} is the fluid velocity vector, p is the pressure, $\vec{\tau}$ is the viscous stress tensor and \vec{F} is the external body force accordingly. In particular, the velocity vector $\vec{V} = V\hat{i} + U\hat{j} + W\hat{k}$ represents the following parameters: V is the component of velocity in the radial direction (which is not accounted for a thin ring-cylinder interface), U is the component of velocity in the axial direction (oil flow entrainment into the ring cylinder clearance) lubricant flow entrainment; and W is the squeeze film velocity.

The stress tensor $\vec{\tau}$ is defined as:

$$\vec{\tau} = \mu \left[(\nabla \vec{v} + (\nabla \vec{v})^T) - \frac{2}{3} \nabla \cdot \vec{v} \vec{I} \right] \quad (7)$$

where μ is the lubricant viscosity and the second term on the right hand side is the effect of volume dilation.

3.2 Boundary conditions

It is initially assumed that, the upper compression ring has the piston velocity, hence the parabola defined by points 1, 2, 3 and therefore the nodes which have a velocity in the axial direction calculated from the relationship (8) and is varied with respect to the angle of the crank.

$$U(\varphi) = -r\omega \sin\varphi \left\{ 1 + \cos\varphi \left[\left(\frac{l}{r}\right)^2 - \sin^2\varphi \right]^{-1/2} \right\} \quad (8)$$

where r is the pin-rod radius, ω is the rotational velocity, l is the rod length and φ is the crank angle.

Similarly, to the previous condition, the nodes belong to the line defined by points 4 and 5 have zero speed. Furthermore, there are two other boundary pressure conditions that define the flow and depend on the direction of compression ring movement or, in other words, the sign of velocity shown in relation 8.

When moving from the BDC to the TDC, the inlet pressure is equal to the pressure inside the cylinder and the outlet pressure is equal to the atmospheric (Fig. 1a), while it is inverted for the movement from TDC to BDC (Fig. 1b).

$$\begin{cases} p(x=b) = \begin{cases} p_{in} = p_{comb} & (BDC \rightarrow TDC) \\ p_{out} = p_{comb} & (TDC \rightarrow BDC) \end{cases} \\ p(x=0) = \begin{cases} p_{out} = p_{atm} & (BDC \rightarrow TDC) \\ p_{in} = p_{atm} & (TDC \rightarrow BDC) \end{cases} \\ p_{bk} = p_{comb} \end{cases} \quad (9)$$

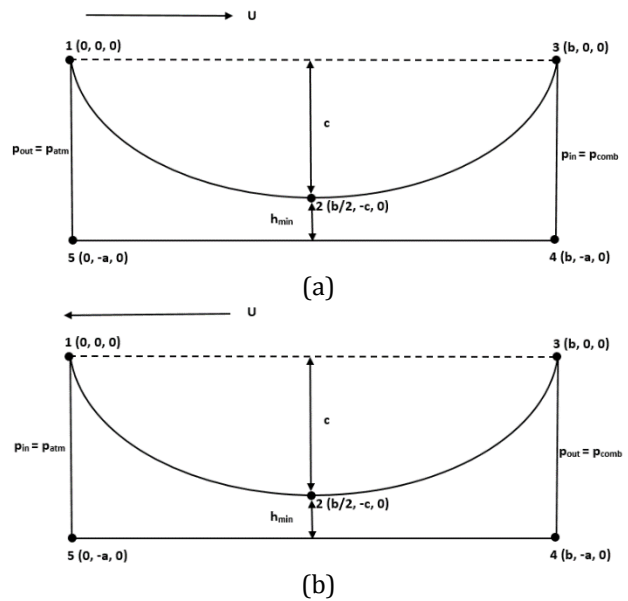


Fig. 1. (a) Boundary conditions for the movement BDC→TDC, (b) Boundary conditions for the movement TDC→BDC.

Finally, it is worth noting that in order to avoid nodes with two overlapping boundary conditions, the velocity conditions are implemented only at the internal nodes of the parabola and the line defined by points 4 and 5, while in the other two lines the pressure conditions are implemented at all nodes, (internal and external). It is also used a condition, known as Half-Sommerfeld, in which the developed negative pressure, derived by the computational solution, is set equal to zero.

Generally, referring to the geometry model presented at Fig. 1, the dimension b is the compression ring thickness, c is the curvature height and a is the maximum distance between the compression ring and the liner at the control volume of lubricant flow.

3.3 Acting forces

In general, the secondary movements of the compression ring can be divided in motions related with the transverse direction, rotation, lifting and twisting. These types of movements stem from various loads acting on the compression ring. These may be inertial loads from ring acceleration or deceleration, damping loads from the lubricant film, loads due to the pressure difference across the ring and frictional forces from slippage along the liner. These forces are shown in Fig. 2. In particular, the gas pressure from above, below and behind the spring produces a force in the cross section of the ring. Inertial forces vary according to the square of the engine speed. The side loading of the piston against the cylinder is a result of the articulated coupling of the rod. In addition, the gap between the liner and the ring has a significant effect on the ring load. Additionally, the shear of the lubricant film, slip friction and contact pressures between the liner and the ring cause tangential forces on the face of the ring. Finally, the elastic deformation of the piston and the liner affects the geometry of the ring profile and the connection of the liner to the cylinder. It causes a non-uniform distribution of the contact pressure, resulting in intense blow-by phenomenon and increased oil consumption [23].

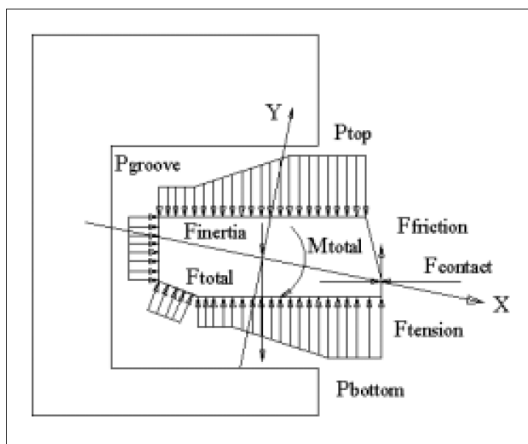


Fig. 2. Acting forces at the upper compression ring [43].

As mentioned in the assumptions section, the forces are considered to be co-planar and radial. The compression ring is subjected to two external forces acting on the inner side of the spring: a resilient force of tension F_{el} and a force from the gases acting behind the ring F_{bk} . It is worth mentioning that these forces are trying to force the ring to fit into the cylinder ($F = F_{el} + F_{bk}$). These forces are calculated as follows:

$$F_{el} = p_{el} \cdot b \cdot (d_{cyl}/2) \quad (10)$$

$$p_{el} = \frac{d_{gap} E_r I_r}{3\pi b \left(\frac{d_{cyl}}{2}\right)^4} \quad (11)$$

$$F_{bk}(\varphi) = 2\pi \cdot b \cdot (d_{cyl}/2) \cdot p_{comb}(\varphi) \quad (12)$$

where p_{el} : pressure due to elastic deformations, d_{cyl} : cylinder diameter, d_{gap} : ring gap, p_{comb} : combustion pressure, $I_r = \frac{bw^3}{12}$: compression ring's inertia moment.

The above external forces are compensated by a contact force consists of a force due to hydrodynamic pressure W_{hyd} and a force due to asperity contacts W_{cont} . The sum of the W_{hyd} and W_{cont} must be equal to the above-mentioned forces. These are computed by formulas (13) and (14) for which the Greenwood-Tripp model is used where E_1 , E_2 correspond to the corresponding elasticity of the liner (or cylinder) and the compression ring.

$$W_{hyd} = \pi d_{cyl} \int_0^b p_{hyd}(\varphi) dx dy \quad (13)$$

$$W_{cont} = \frac{8\sqrt{2}}{15} \pi (\zeta \kappa \sigma_{rms})^2 \sqrt{\frac{\sigma_{rms}}{\kappa}} E' A F_{5/2}(\lambda) \quad (14)$$

$$A_{cont} = \pi^2 (\zeta \kappa \sigma_{rms})^2 A F_2(\lambda) \quad (15)$$

$$\frac{1}{E'} = \frac{1}{2} \left(\frac{1-\nu_1^2}{E_1} + \frac{1-\nu_2^2}{E_2} \right) \quad (16)$$

$$F_{5/2}(\lambda) = -0.0046\lambda^5 + 0.0574\lambda^4 - 0.2958\lambda^3 + 0.7844\lambda^2 - 1.077\lambda + 0.6167 \quad (17)$$

$$F_2(\lambda) = -0.0018\lambda^5 + 0.0281\lambda^4 - 0.1728\lambda^3 + 0.5258\lambda^2 - 0.8043\lambda + 0.5003 \quad (18)$$

where $\zeta \kappa \sigma_{rms}$: roughness parameter, σ_{rms}/κ : asperity gradient, $\sigma_{rms} = \sqrt{\sigma_1^2 + \sigma_2^2}$: mean square of finishing of the two surfaces, E' : equivalent elasticity modulus of the two surfaces, A : area of smooth contact surface, $F_{5/2}$, F_2 : probability distribution of asperities height as 5th order polynomial function, $\lambda = h/\sigma_{rms}$: Stribeck parameter.

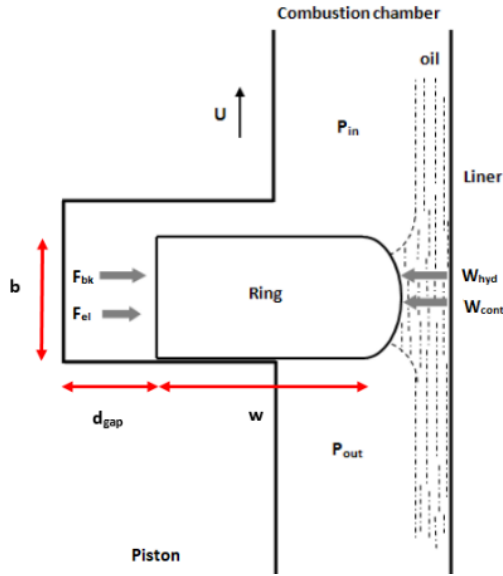


Fig. 3. Acting forces on the compression ring.

In this section, it is noted that after the developed pressure from the CFD model and the convergence of the criteria, mentioned in section 4.2 (see below), are met, friction and energy losses can be found. The friction consisting of shear viscosity and asperity contact friction (mixed/boundary friction) is given by (19).

$$F_{fr} = \left| \pm \frac{h_{min}}{2} \nabla p - \Delta \vec{W} \frac{\mu}{h_{min}} \right| (A - A_{cont}) + \tau_0 A_{cont} + \mu_{asp} W_{cont} \quad (19)$$

where $\tau_0 = 2 \cdot 10^6$ Pa: Non-Newtonian Eyring shear stress of the lubricant [25], $\mu_{asp} = 0.17$: boundary shear strength of surfaces with ferrous-based oxide layer [25].

The power of the friction losses arises if the relation (9) is multiplied by the velocity U that depends on the angle of the crank.

$$P_{fr} = F_{fr} \cdot U(\varphi) \quad (20)$$

4. NUMERICAL ANALYSIS

4.1 Mesh creation

The mesh creation is presented in this paragraph. The appropriate FLOTTRAN CFD element, which refers to solving the momentum equations coupled with the continuity equation, FLUID141 is used, in order to create the solution mesh (Fig. 4).

Specifically, the resulting velocities are calculated from the principle of mass

conservation and the pressures from the momentum conservation principle. This particular type of element is also used to solve thermal problems, other than fluid properties, by solving in addition the energy equation. The fluid dynamics problem is nonlinear in general and the above equations (mass conservation and momentum conservation principle) are coupled making use also of the SIMPLE (Semi-Implicit Method for Pressure Linked Equations) algorithm. The solution of all these equations, including the re-calculation of any temperature or pressure-dependent property, is a global iteration. A number of iterations are required in order to achieve convergence for the solution. This may vary depending on the size of the mesh (number of elements and nodes) and the stability of the algorithms itself. In addition, the degrees of freedom of this element are the velocity, the pressure and the temperature.

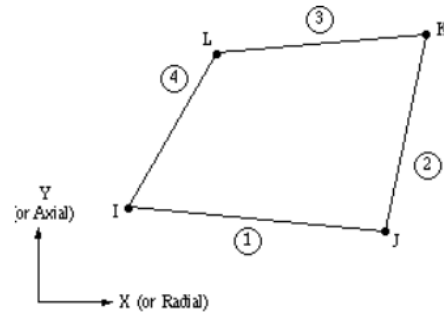


Fig. 4. FLUID141 2-D Fluid-Thermal Element [26].

4.2 Convergence criteria

Two types of convergence criteria are used in this analysis. The first criterion referring to the pressures depends on the discretization of the Navier - Stokes equations and the continuity equation in order to extract the hydrodynamic pressure. This criterion that has to be met is:

$$Error_{press} = \frac{\sum_{i=1}^{N_{CFD}^n} |p_i^k - p_i^{k-1}|}{\sum_{i=1}^{N_{CFD}^n} |p_i^k|} \leq 10^{-6} \quad (21)$$

The second criterion concerns the quasi-static equilibrium of the forces shown in Figure 3. If this condition is satisfied then the algorithm renew the value of the minimum lubricant thickness h_{min} , and both, the last pressure p_{hyd} and the last minimum lubricant thickness h_{min} values are used. This criterion which is referred to forces calculation ca be expressed as:

$$Error_{load} = \left| \frac{F-W}{F} \right| \leq 10^{-3} \quad (22)$$

If the criterion (22), is not satisfied then the algorithm takes care to renew the value of the minimum lubricant thickness h_{min} following the formula below (23):

$$h_{min}^{new} = (1 + \delta X)h_{min}^{old} \quad (23)$$

where $X = \frac{F-W}{\max\{F,W\}}$ and $\delta = 0.05$, is the relaxation factor for solution stability.

4.3 Mesh Sensitivity tests

After the sensitivity analysis shown in Fig. 5, the geometry of the model (see Fig. 1) is divided into 1000 elements at the axial direction and at the radial into 15 elements, i.e. a 1000x15 mesh size. These elements are quadrilateral finite elements and in the ANSYS APDL environment, free mesh method is used.

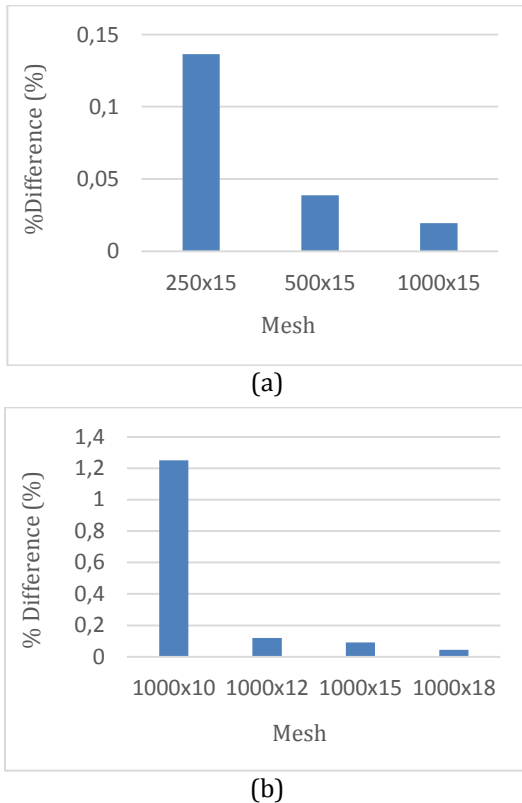


Fig. 5. Mesh sensitivity analysis.

5. EXPERIMENTAL PROCEDURE

5.1 Experiment description

The purpose of the experiment was to collect acoustic measurements from an engine and process them using several processing techniques. To this end, a single-cylinder four-

stroke and air cooled internal combustion engine using gasoline as a fuel was used, to carry out the measurements. The engine manufacturer is Lifan and its volume is 107 cubic centimeters. More technical features are shown in Table 1 [33].

Table 1. Technical specifications of experimental engine.

| Parameter | Value | Unit |
|---|-------------------------|---------------|
| motorbike engine type | four stroke, air cooled | — |
| motorbike volume | 107 | cc |
| nominal cylinder diameter, D_{cyl} | 0,0524 | m |
| crank-pin radius, r | 0,025 | m |
| rod length, l_{rod} | 0,096 | m |
| rotational speed, Ω | 1000-1500 | rpm |
| compression ring thickness, b | 0,0005 | m |
| compression ring width, d | 0,002 | m |
| piston-ring end gap, d_{gap} | 0,00015 | m |
| compression ring material | Chromium plated | — |
| Young's modulus of elasticity for ring, E_r | 2,76E+11 | GPa |
| compression ring poisson's ratio, ν_r | 0,21 | — |
| thermal conductivity, k_r | 93,9 | W/mK |
| specific heat capacity, c_{rp} | 448 | J/KgK |
| cylinder block material | Aluminum | — |
| Young's modulus of elasticity for cylinder, E_{cyl} | 70 | GPa |
| cylinder Poisson's ratio, ν_{cyl} | 0,33 | — |
| thermal conductivity, k_{cyl} | 273 | W/mK |
| specific heat capacity, c_{pcyl} | 904 | J/KgK |
| roughness parameter, $(\zeta\kappa\sigma)$ | 0,04 | — |
| asperity slope, (σ/κ) | 0,0015 | — |
| ring roughness (μm) | 0,2 | μm |
| cylinder (μm) | 0,15 | μm |
| curvature height | 15 | μm |

The engine for the measurements is set to operate at 1000 rpm and the pressure distribution inside the cylinder during a complete engine cycle is shown in Fig. 6.

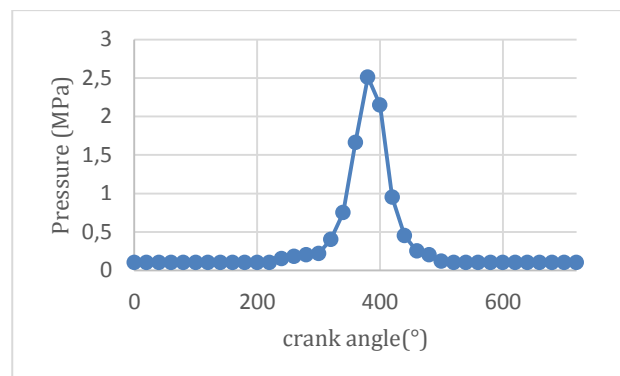


Fig. 6. Pressure distribution along crank angle for an engine cycle [33].



Fig. 7. View of the experimental engine.

Referring to the measurement hardware, a pre-stressed condenser microphone ½ " SV12L is used [27].



Fig. 8. SV12L condenser microphone.

NI cDAQ-9188 (DAQ) produced by National Instruments is used to collect data [28].



Fig. 9. NI cDAQ 9188.

5.2 Experimental setup

The experimental setup includes the microphone mounted on various engine positions, the DAQ system and the LabView software on the computer.

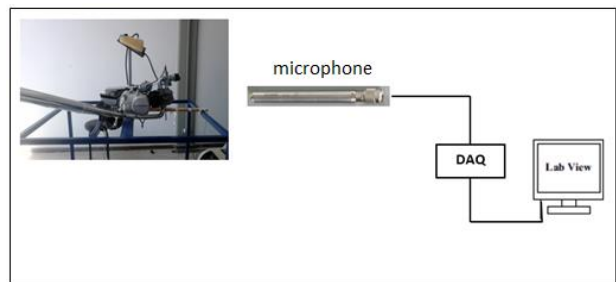


Fig. 10. Diagram of experimental setup.

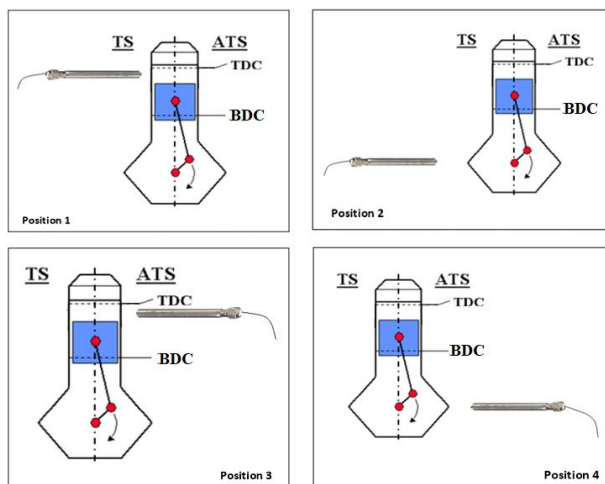


Fig. 11. Positions of the microphone at the engine.

The aim of this study is to determine the main sources of mechanical noise, whose causes also induce friction, emphasizing on the piston slap which is the largest of them. For this reason, a sampling frequency equal to 12800 Hz is selected, so as to diagnose all phenomena, especially the mechanical ones. Measurements are conducted on both thrust (TS) and antitrust (ATS) side. The positions selected for the acoustic measurements are shown in Fig. 11 and the distance from the engine block is set to 40 cm. In particular, the TDC is selected because the maximum piston slap is appeared on this position. Moreover, measurements of the acoustic field are conducted near the crankshaft, in order to separate them from induced noise by the piston ring.

6. NUMERICAL RESULTS

6.1 CFD Validation

The CFD model, which was created in the APDL environment of the ANSYS program in FLORTRAN language, was tested for its validity with the results of the publication of Shahmohamadi H. et al. [19].

Based on the data presented in the above mentioned publication [19], the following pressure diagrams along the compression ring profile (curve defined by points 1, 2, 3, Fig. 1) and pressure distribution figures at the parabolic wedge (model) with color variations produced via ANSYS APDL. In particular, some characteristic crank angles were tested which are: $\pm 1^\circ$, $\pm 21^\circ$, $\pm 90^\circ$ under isothermal conditions and quasi-static equilibrium. It is noted that for a

crank angle equal to 0° the compression ring is in the position of TDC, in the transition from the compression stroke to the combustion one. Observing the shapes for the pairs of symmetrical angles mentioned earlier, inlet reversal is observed, that is the maximum pressure for negative degrees being in the right half of the parabola, while for positive angles it is at the left half. More specifically, at angles equal to -1° and 1° the difference between the maximum developed pressures of the current work and of the ref. [19] are 2.5 % and 0.1 % respectively. Furthermore the case where the angle is 21° corresponds to the moment of combustion and the release of power. This is why the maximum pressure is reasonably appeared and is equal to 23.4 MPa, which has a difference of 1 % comparing to the maximum pressure in the relative publication [19]. In addition for the symmetrical angle of -21° the difference is 6.5 %. The third set of angles corresponds to low loads, where the piston is in the middle of the stroke. At angles -90° and $+90^\circ$ the difference is 2.8 % and 6 % respectively. Overall, these representative results are consistent with those of publication [19], so the developed code is valid.

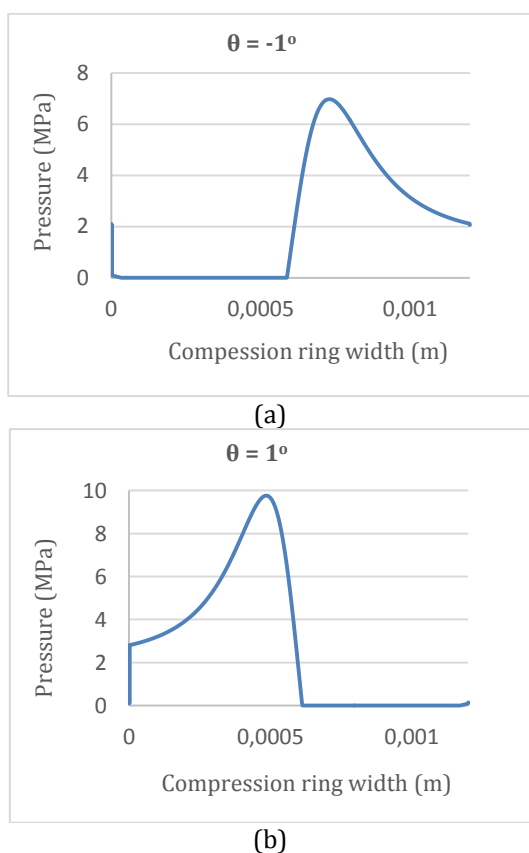


Fig. 12. Pressure distribution figures from the profile of compression ring (spline defined by 1,2,3 points) for crank angles $\pm 1^\circ$.

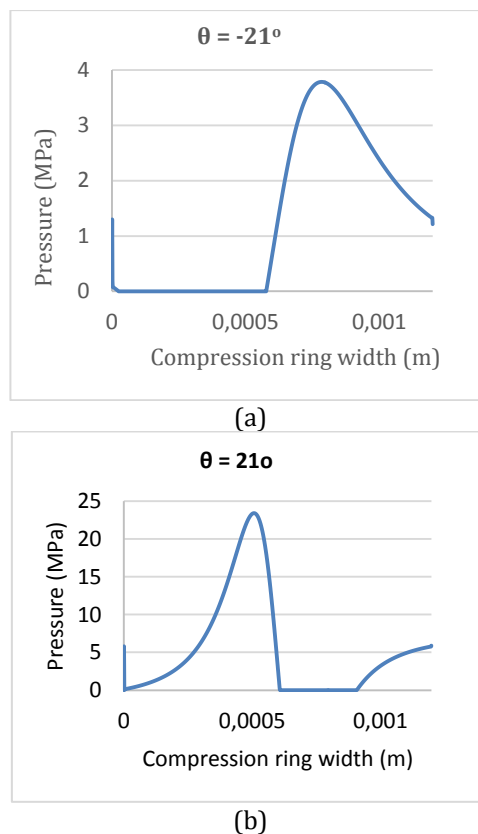


Fig. 13. Pressure distribution figures from the profile of compression ring (spline defined by 1,2,3 points) for crank angles $\pm 21^\circ$.

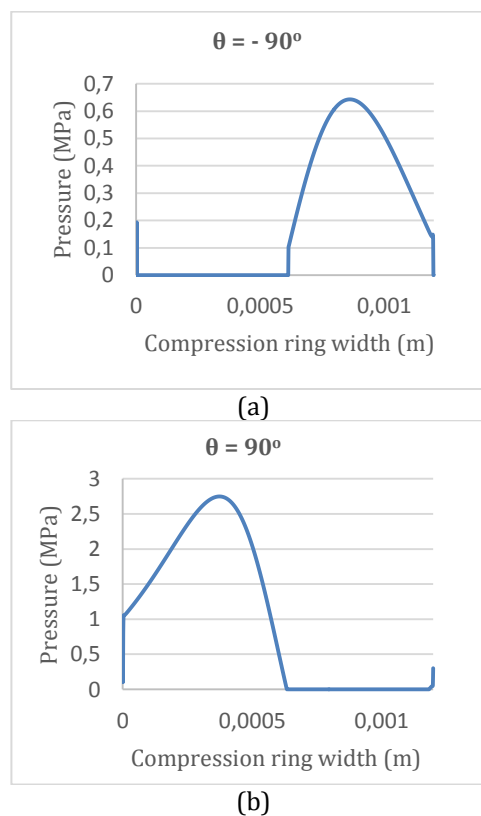


Fig. 14. Pressure distribution figures from the profile of compression ring (spline defined by 1,2,3 points) for crank angles $\pm 90^\circ$.

6.2 Compression piston ring noise

Further to successful validation of the developed CFD model, the code was applied for the experimental engine Lifan 107cc [33] using the technical characteristics shown at the Table 1. In this case the combustion takes place just before the 365° of the crank angle, therefore the minimum lubricant thickness and the maximum developed hydrodynamic pressure are expected to occur in this angle.

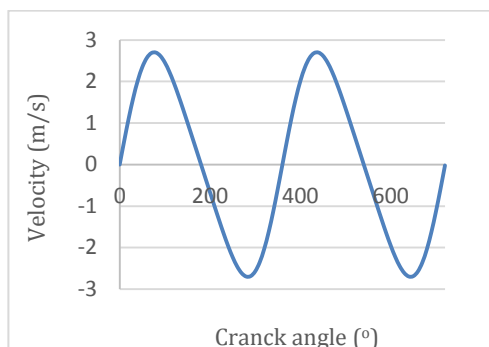


Fig. 15. Piston velocity against crank angle for Lifan 107cc at 1000 rpm.

Table 2. Lubricant properties SAE 30 at atmospheric pressure and temperature 40 °C.

| Parameter | Value | Units |
|-------------------------------------|--------------------|-------------------|
| Lubricant's density, ρ_0 | 858 @ 40 °C | kg/m ³ |
| Lubricant's dyn. viscosity, μ_0 | 0.075 @ 40 °C | Pa/s |
| Specific heat, c_p | 1985 | J/kgK |
| Thermal conductivity, k | 0.143 | W/mK |
| α_0 | 1×10^{-8} | m ² /N |
| β_0 | 4×10^{-2} | |

Based on the data provided in Table 1, and Figs. 6, 15, the following pressure diagrams along the compression ring's profile (curve defined by points 1,2,3 as shown in Fig. 1) and pressure distribution diagrams in the region of the parabolic wedge are presented. The color variations were produced by CFD analysis. In particular, the corresponding figures are depicted for the cases of crank angles in pairs: 358° and 361°, 365°, 290° and 450° under isothermal conditions and quasi-static equilibrium. It is noted that for a crank angle of 360° the compression ring is in the position of the TDC, during the transition from the compression stroke to the combustion stroke. Observing the shapes of the pairs of the symmetrical angles mentioned earlier, inlet reversal is also noticed. Moreover, the case where the angle is 365° corresponds to the

moment of combustion and the release of power. This is because, of the maximum pressure appeared to be 8.08 MPa. The third set of angles corresponds to low loads where the piston is in the middle of the stroke and therefore the maximum pressure is lower than that after combustion ($\theta = 365^\circ$).

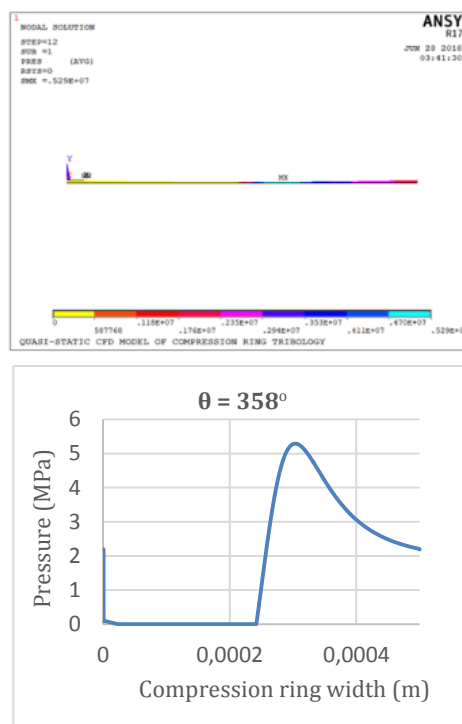


Fig. 16. Pressure distribution in the wedge parabola (left) and pressure on the compression ring's profile @ 358°.

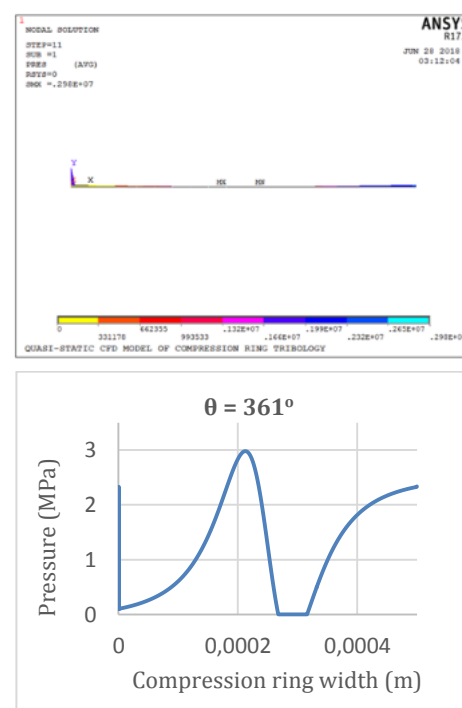


Fig. 17. Pressure distribution in the wedge parabola (left) and pressure on the compression ring's profile @ 361°.

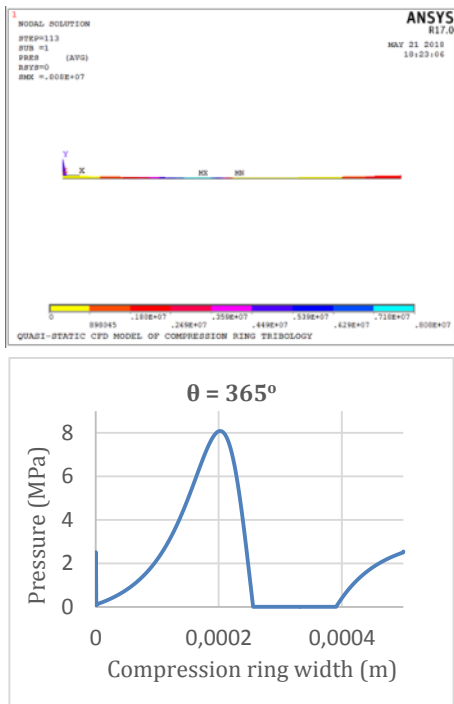


Fig. 18. Pressure distribution in the wedge parabola (left) and pressure on the compression ring's profile @ 365°.

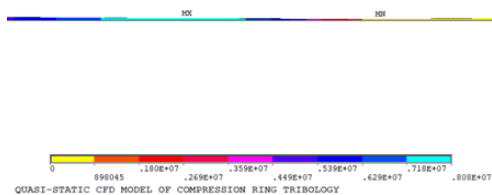


Fig. 19. Zoom at the region of the maximum developed pressure @ 365°.

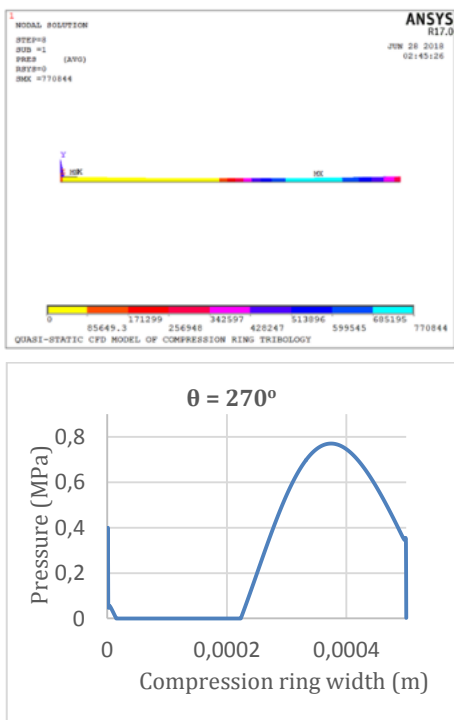


Fig. 20. Pressure distribution in the wedge parabola (left) and pressure on the compression ring's profile @ 270°.

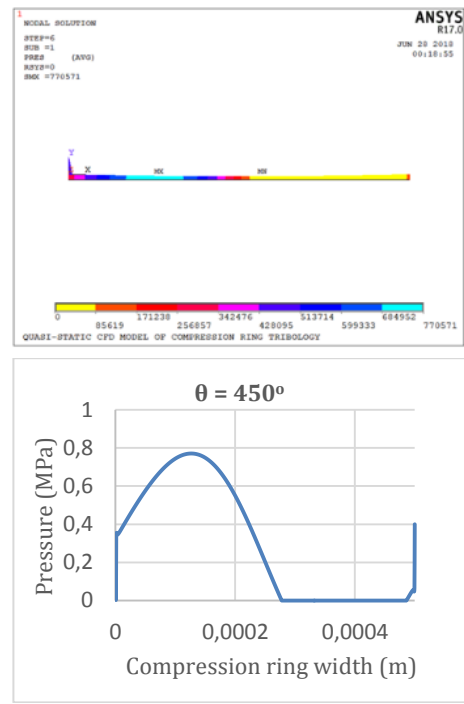


Fig. 21. Pressure distribution in the wedge parabola (left) and pressure on the compression ring's profile @ 450°.

Beyond of the above characteristic solutions, the CFD code was applied for every crank angle for a complete engine cycle, and the computed minimum lubricant thickness for each position of crankshaft is presented in Fig. 22. From this figure, it is obviously that at angle equal to 365°, the total minimum lubricant thickness is clearly shown just after the combustion stage. Also, the rest of the local minima corresponds to the dead centers, which is reasonable, because in these areas the lubrication regime is mixed/boundary. In addition, the local maxima corresponds to the middle of the piston's motion from TDC to BDC and from BDC to TDC, thus the minimum lubricant thickness is maximized. This is due to the fact that the hydrodynamic lubrication is predominant and the piston velocity is very high.

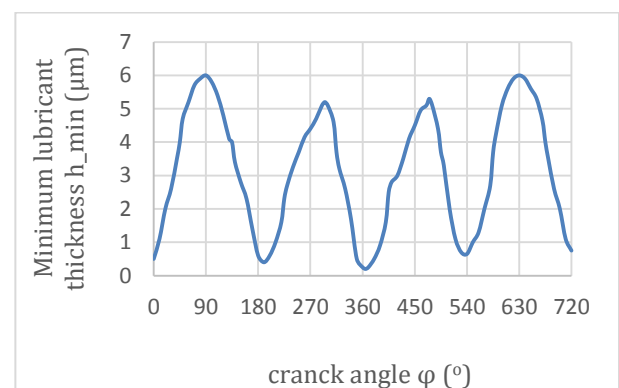


Fig. 22. Minimum lubricant thickness along crank angle.

In addition, the total developed friction is computed involving the viscous friction due to shear and the asperity contact friction as mentioned in section 3.3. Concerning the figure 23, it is observed that at the angle of 365°, after the combustion, a maximum friction of 49.35 N is developed. Furthermore, the shape of the diagram is generally in agreement with the experimental results (Fig. 11c [20]) of Mishra et al. [20], so this diagram is valid. Also, in Figure 23, the dominant effects of the individual terms of friction are noted. It is noted that the maximum friction is affected mainly by Poiseuille flow (influence of combustion pressure) with the simultaneous effect of asperities (mixed / boundary lubrication). At the remaining areas, viscous friction due to Couette flow dominates which is proportional to velocity (second term of viscous friction in relation (19)).

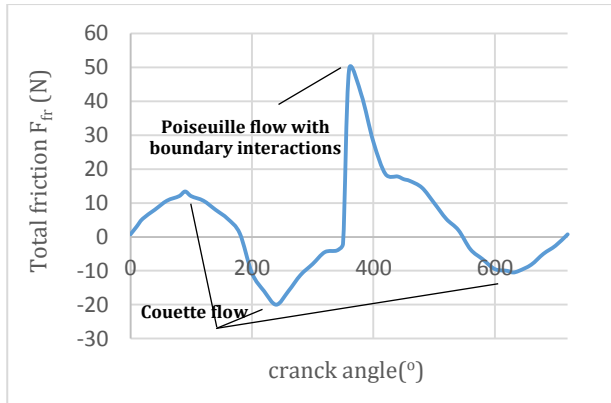


Fig. 23. Total friction for each crank angle.

Figure 24 shows the power losses due to friction, computed by equation (10) where it is notified that the maximum energy loss is 56.4 W.

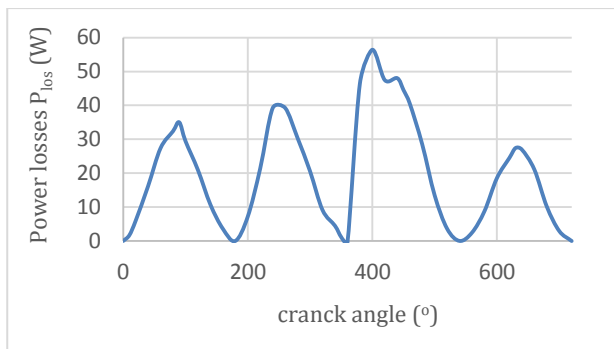


Fig. 24. Power losses versus crank angle.

In this work, a method for predicting SPL value of compression ring's interaction with the liner is proposed. The SPL value can be predicted if the ratio of structural attenuation ratio $\eta_{a/v}$ is

known. This quantity is used to predict the loss of energy of acoustic wave through the engine block structure. The structural attenuation ratio is the ratio of the acoustic power P_a divided by the force that vibrates the structure (impact power) P_v and is given by the equation (24).

$$\eta_{a/v} = \frac{P_a}{P_v} \quad (24)$$

According to Ungar and Ross [29] for aluminum cylinders this ratio equals $12 \cdot 10^{-5}$. As structure's excitation power, the power produced by the friction losses is used since the friction is a cause of vibrations. Therefore, the acoustic power is extracted from the solution of the equation (24). Then, the equation (25) is used, for the sound power level calculation, as follows:

$$L_W = 10 \log \frac{P_a}{P_{ref}} \quad (25)$$

Where $P_{ref} = 10^{-12}$ W. Knowing the sound power level, the SPL sound pressure level can be calculated from type (26).

$$SPL = L_W + 10 \log \left(\frac{\bar{s}_0}{4\pi R_b^2} \right) \quad (26)$$

Where \bar{s}_0 represents the characteristics of the acoustic field and it is known that $\bar{s}_0 = 1$ for free field and $\bar{s}_0 = 2$ for hemispherical acoustic field and R_b is the distance from the motor.

Thus, using the values of P_{loss} in Fig. 24 which represents the power losses due to friction and setting $\bar{s}_0 = 1$ and $R_b = 1$, the sound pressure level for each crank angle shown in Fig. 25 is calculated. It is found that, the maximum value of the SPL is 86 dB and it is near to combustion. Furthermore, it seems reasonable that at the dead centers, SPL is almost zero since the velocity is zero, and just then rises sharply until it gets its maximum SPL value as piston goes to combustion stroke.

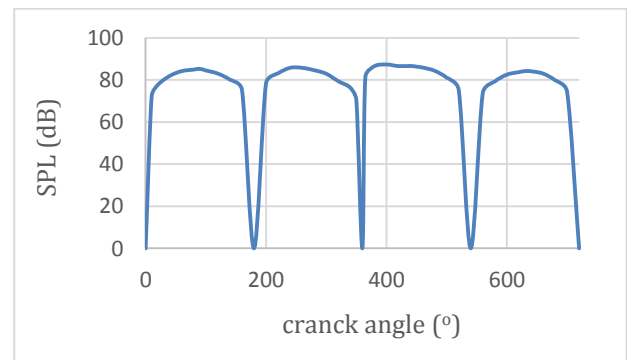


Fig. 25. Predicted SPL value due to friction for each crank angle.

6.3 Cranckshaft Noise

In this paragraph the pressure distributions at specific crank angles are calculated based on the equation 4.33 [37], following the narrow bearing approximation for simplicity [37]. The specifications of the crankshaft bearing are shown in Table 3.

Table 3. Specifications of the crankshaft bearing.

| Parameter | Value | Units |
|-----------------------------------|-------|---------------|
| Radius, r | 0.025 | m |
| Length, l | 0.025 | m |
| Eccentricity, ϵ | 0.15 | - |
| Eccentricity parameter, c_r | 50 | μm |
| Lubricant's dyn. viscosity, μ | 0.05 | Pa/s |

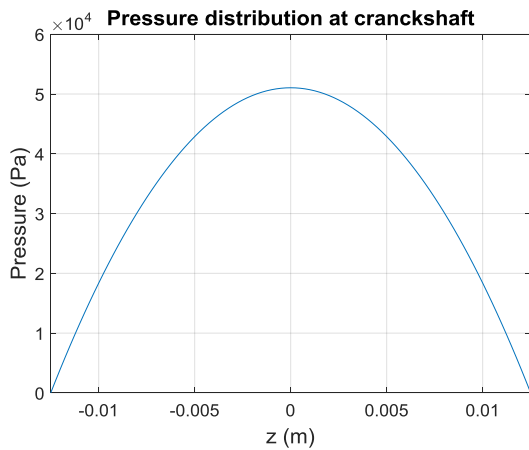


Fig. 26. Pressure distribution of lubricant along the crank bearing @ 30°.

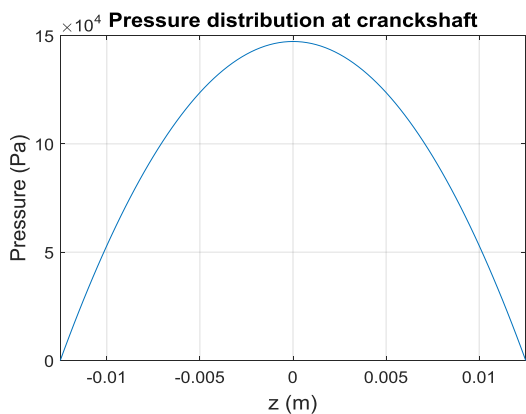


Fig. 27. Pressure distribution of lubricant along the crank bearing @ 90°.

The pressure distribution diagrams are presented at Figs. 26, 27 and 28 assuming narrow crankshaft bearings for crank angles equal to 30°, 90° and 270° respectively. It is noted that these diagrams follow the parabolic

distribution and the maximum pressure occurs at the middle of the bearing. The cases for 90° and 270° are the positions in which the microphone was located during the acoustic measurements towards crankshaft, and gave the largest contribution without diffusion. These degrees were also chosen due to maximum pressure distribution and further the possibility of maximum noise generation.

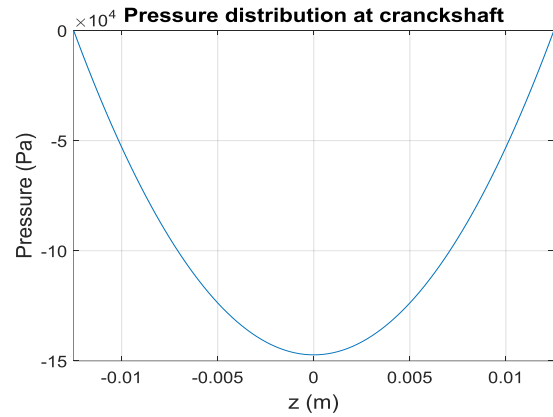


Fig. 28. Pressure distribution of lubricant along the crank bearing @ 270°.

Simultaneously, having the pressure distribution inside the bearing, the SPL value is predicted in the air making the assumptions concerning the narrow bearings. According to B-H Rho, D-G Kim, K-W Kim [38], it can be seen that changes in lubricant pressure results in noise emission, even in the form of plane waves. Subsequently, can be pointed out, the notion that the acoustic wave propagates in the radial direction, through the bearing, and that the energy losses are negligible. In addition, it is assumed that the acoustic pressure of one medium at the boundary between the two propagating media is the same as that of the other medium and correspondingly the particle velocities at the boundary of the two media are equal. Then, the propagating wave p_2 maintains the direction of the interpolated p_1 and is given by the formula (27) [31]. In particular, the material properties shown in Table 4 are used in order to calculate the acoustic impedances. After calculating these quantities, SPL of the bearing is calculated applying the equation (28) [31]. It is noted that the reference pressure in order to calculate the SPL value is 20 μPa .

$$p_2 = p_1 \frac{2z_2}{z_1 + z_2} \quad (27)$$

where $z_1 = \rho_1 \cdot c_1$: acoustic impedance of medium 1, $z_2 = \rho_2 \cdot c_2$: acoustic impedance of medium 2.

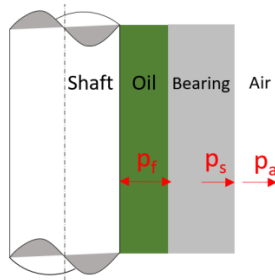


Fig. 29. Transmission of plane waves at a rotor-bearing system [38].

If f, s, a are used as subscripts to represent the acoustic sizes of the lubricant, bearing (steel) and air respectively, then the acoustic pressure in air is given by:

$$p_a = p_f \frac{2z_s}{z_f+z_s} \frac{2z_a}{z_s+z_a} \quad (28)$$

Table 4. Material properties of the media in which the acoustic wave is transmitted.

| Parameter | Value | Units |
|---------------------------------|-------|-------------------|
| Air density, ρ_a | 1.18 | kg/m ³ |
| Sound speed in air, u_a | 344 | m/s |
| Steel density, ρ_s | 7700 | kg/m ³ |
| Sound speed in steel, u_s | 5050 | m/s |
| Lubricant's density, ρ_f | 833 | kg/m ³ |
| Sound speed in lubricant, u_f | 1461 | m/s |

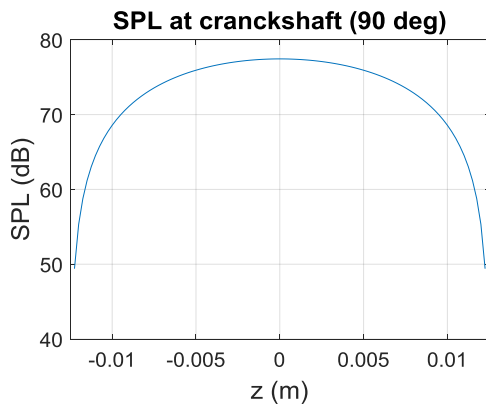


Fig. 30. Computed SPL value of the cranckshaft bearing @ 90°.

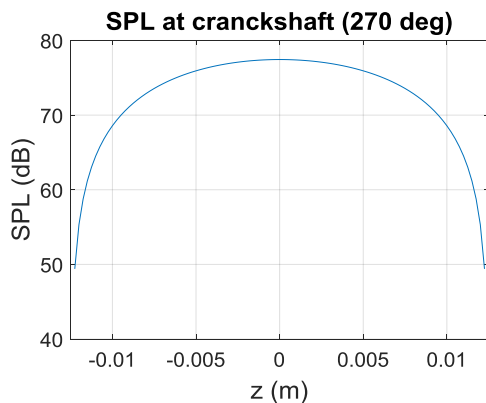


Fig. 31. Computed SPL value of the cranckshaft bearing @ 270°.

The measurements were conducted at 40cm distance from the emission point. Then, as the sound pressure of the free filed level decreases with the distance, it is calculated by removing from the actual value the logarithm of the ratio of the measurement distance over the reference distance, by multiplied overall by 20 [31]. The maximum computed sound pressure level is 77.96 dB due to pressure fluctuations while the minimum is 47.96 dB.

7. WAVELET ANALYSIS OF THE EXPERIMENTAL RESULTS

6.1 Piston ring

The signals for duration of 30 s for positions 1 and 3 are shown in Figs. 32 and 33 respectively and the relevant signals removing the mean value are shown in Figs. 34 and 35 in order to remove the effect of mean value from the results.

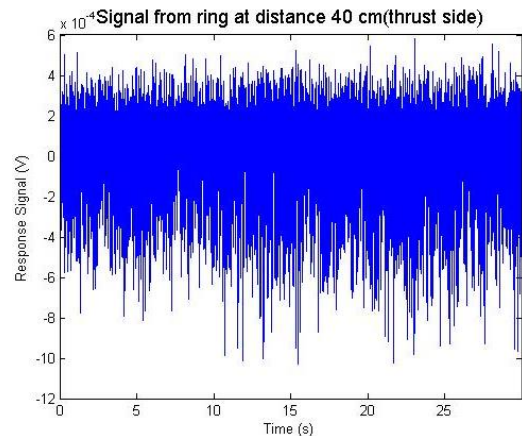


Fig. 32. Signal from position 1.

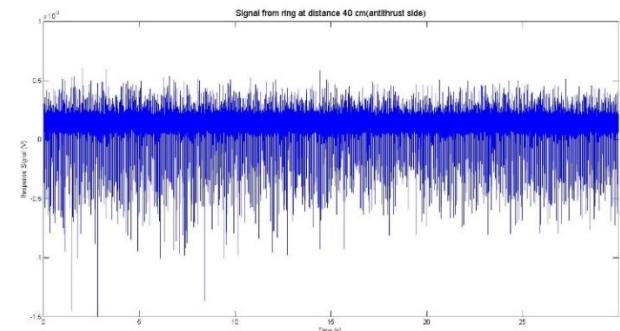


Fig. 33. Signal from position 3.

From Fig. 32 and 33, it can be noticed that the signals for positions 1 and 3 are strongly stochastic. Apparently, all values of the original signal (without detrend) range around a constant value. So, it seems to have a constant mean value.

It is also shown, that in the signals the variance is not stable and is time-dependent. However, it changes in a periodic way. Consequently, observing that the signal has a constant mean value and furthermore the autocovariance is a time dependent and periodic variable, it is estimated that the signal is non-stationary, and furthermore due to its periodicity becomes cyclostationary. It is stated that, autocovariance function plays an important role in time series analysis and it can be often used to study the underlying dependence structure of the process, Ansley [31]; Brockwell and Davis [32]).

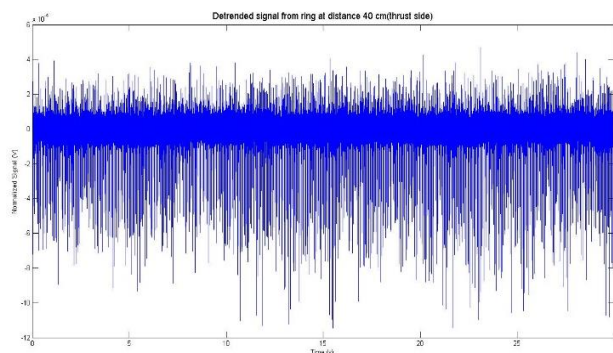


Fig. 34. Signal from position 1 removing the mean value.

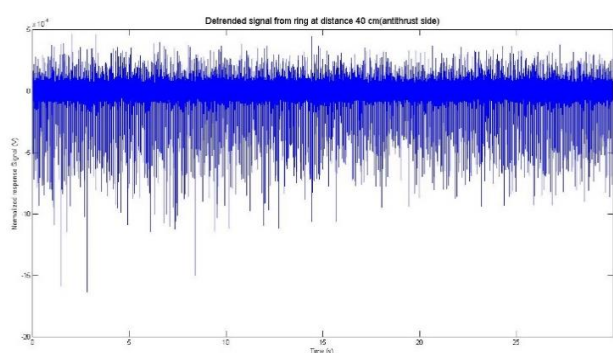


Fig. 35. Signal from position 3 removing the mean value.

The transition from the time domain to the frequency domain is based on the Fourier transform. The FFT (Fast Fourier Transform) frequency range is from zero (0) to the sampling frequency but due to the symmetry (DFT or FFT magnitude), the graph is displayed up to half the sampling frequency (Nyquist frequency). Therefore, from the FFT transform, the signal in the frequency domain is displayed up to a frequency of 6400 Hz. The frequency step is given by the formula $\Delta f = f_s/N$. In this paper, the sampling frequency is $f_s = 12800$ Hz and N is the number of segments, that is, in this case the entire signal, which includes 384000 samples, with frequency resolution equal to 0.0333.

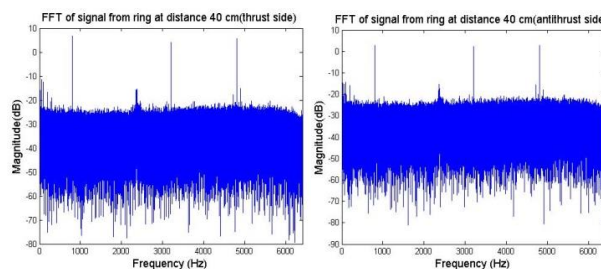


Fig. 36. Absolute value of Fast Fourier Transform (FFT) for the position 1 (left) and 3 (right).

From Fig. 36, the system's eigenfrequencies can be extracted. Despite the fact that, the Fourier transform presents the frequency content of the system, it is not able to detect the frequency content of transient phenomena and especially the frequency occurred by impulsive phenomena. It is also important during the diagnosis of a CI/SI engine to project the time apart from the frequency, because the tribological phenomena, in which there is solid-solid contact, are stochastic and their significance varies according to the position of piston (or compression ring) in a CI/SI engine. It is therefore recommended to use a technique that shows the signal in the combined time-frequency domain.

As mentioned previously in Paragraph 2, the wavelet transform provides the ability to present the signal in a combined time and frequency domain. An important question is the choice of the appropriate mother wavelet. According to the literature in the diagnostic of machines, it is common to use the Morlet wavelet because it can better diagnose impulse signals, due to its shape, and has the ability to display both the measure and phase of the transformation and thus provides useful information. Moreover, its envelope is a Gaussian distribution and therefore detects impact parts of a signal since the usual symptoms of faults/damages in mechanical systems are impulse signals. In this paper, continuous wavelet transform (CWT) is used, because it is interesting to accessed all the scales and to have a high time resolution at all scales since the wavelet is smoothly shifted along the length of the signal.

Because the phenomena in an internal combustion engine are very fast and impulsive, it is observed in the signal, that there is a specific continuous time period in which a very high-

energy impulsive signal is being appeared, which represents the combustion phase in the engine cycle. Between two combustions the remaining phenomena are happening within an engine cycle corresponding to two crankshaft rotations or four strokes of the engine.

In this work, a part of the whole signal length is presented which includes four combustions stages. Figure 37 is presented involving the coefficients of the CWT transformation where the vertical axis represents the scales, while the horizontal represents the time. Due to the fact that the scale parameter indirectly represents the frequency, Fig. 36 illustrates the CWT transformation including frequency and time, and it is noted that the red arrows show the 4 combustions. It is worthy saying that between two consecutive combustions the time interval is stable and is equal to the timing of the engine. In these diagrams (37-38), wavelet coefficients are distinguished on each scale according to color and on this basis their values is given (see color bar on the right). The red color corresponds to high energy phenomena while cyan in less ones. To extract all of the graphs presented in this paper, the scales range from 1 to 10 in 0.001 increments.

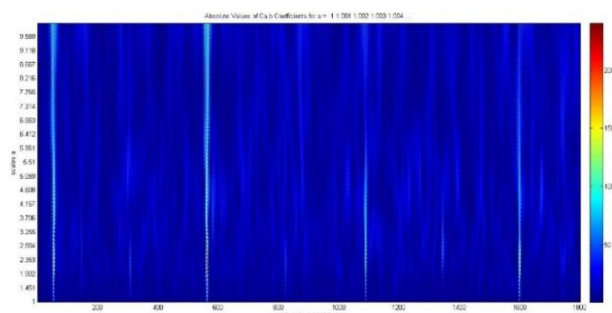


Fig. 37. Continuous wavelet transform (CWT) for scales [1,10] and step 0.001 for the position 1.

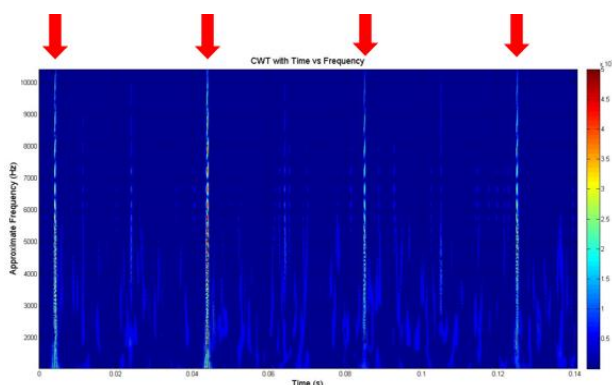


Fig. 38. Frequency – Time diagram of continuous wavelet transform (CWT) for scales [1,10] and step 0.001 for the position 1.

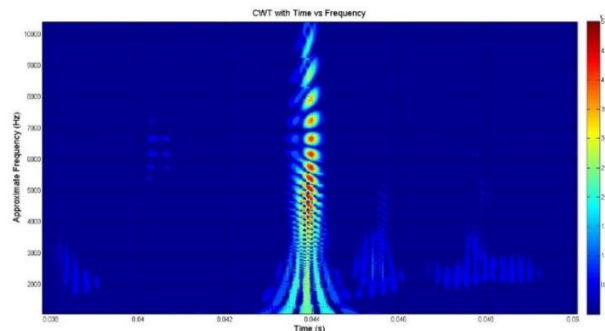


Fig. 39. Zoom of the figure 35 on the combustion region.

Figure 39 shows an enlarged view of the combustion area and an impulse is observed, therefore it can be easily alleged, according to Liu X., Randall R.B. [23], that the noise due to combustion is a super-Gaussian source. Due to the fact that the phenomenon of combustion and the dominant phenomenon of the mechanical noise, piston slap, are overlapped at the TDC, the two phenomena will be separated considering the frequency band observed in the literature and taking as an indication that the noise source due to the secondary piston movement is sub-Gaussian [17]. The zoom of the combustion provided by Fig. 39 is also observed to be uniform but oscillating due to the different cylinder volume (gas and air mixture) over time. Furthermore, at higher frequencies, appearance of large energy holes is observed, corresponding to turbulent flow during combustion and logically representing both heat transmission and noise and vibrations. For this reason, an analyst could assume that the appearance of these high energy cycles is a source of noise due to the combustion knock. This phenomenon is common in spark ignition engines.

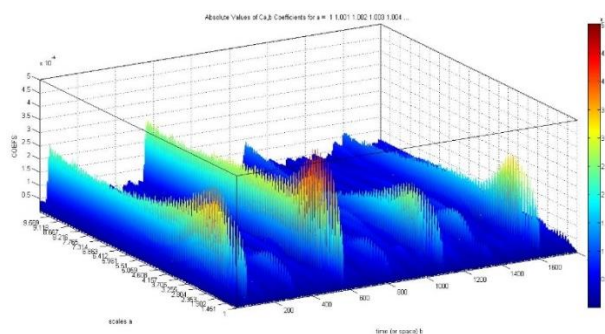


Fig. 40. Three dimensional representation of CWT for scales [1,10] and step 0.001 for the position 1

Figure 40, shows the three-dimensional representation of Fig. 38, which clearly presents that the large peaks, containing the red color, are the four combustions. The other peaks represent other phenomena within the four strokes of the

engine except for combustion, for which it is necessary to filter properly. This presentation of CWT demonstrates the ability of the wavelet transform to decompose the signal into its components and to display the acoustic signal produced by each source. In order to remove contributions from other sources of energy, which are of minor importance, it is necessary to create a filter. The present work aims to find noise sources due to friction or, more generally, impact forces at the interaction of piston assembly, lubricant and cylinder liner giving more emphasis on piston slap. Some researchers have identified the frequency range of mechanical noise (due to friction) at the band 400-3200 Hz [30]. Other researchers [17] suggested 1000 - 3000 Hz while Nakashima K. et al. [18] suggested 500-2000 Hz. However, this work agrees with publications [15-16] in which the band of 450 - 3500 Hz was used. In particular, an IIR filter of the type is Chebyshev Type I of the 10th order.

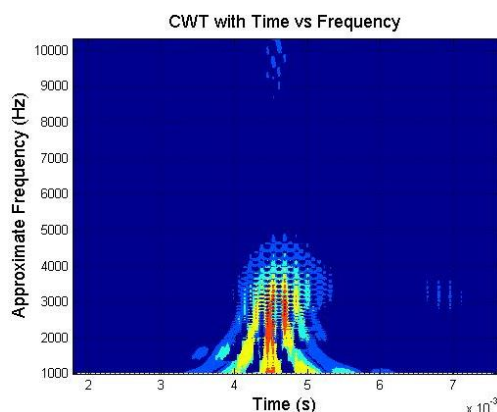


Fig. 41. CWT of the combustion region applying bandpass filter [450-3500Hz] for position 1.

The largest piston slap event occurs at the moment of combustion (beginning of the expansion stroke) where the inertial forces and forces from the increased pressure inside the cylinder are maximum within an engine cycle. By removing the combustion and filtering the signal as shown in Fig. 42, the remaining events occurring within the four strokes of an engine can be more accurately determined giving more emphasis on the piston slap events because it contains the greatest energy and thus gives the major contribution to mechanical noise. Similar methodology is followed for the other three positions of the microphone. It is observed that the piston slap, appeared just before the time of 0.025 sec at position 1 and 0.065 sec at position 3, contains the most energy and is in a wide enough frequency range and has a long

duration. This is reasonable, because at this position another noise source associated with the impact load exerted by the closing of exhaust valve at the end of the exhaust stroke contribute to the overall noise as stated in the publication of Dolatabadi N. et al. [18]. Except of this moment, the opening or closing of the valves also contributes to piston slap events at various times. Overall, according to Dolatabadi N. et al. [18] 20 piston slap events were identified based on angle duration and 13 piston slap events were identified using the maximum energy transfer method. Generally, due to the fact that the piston slap is a strongly non-stationary phenomenon, it cannot be accurately predicted as piston strikes from one side to the other continuously. This movement depends on engine speed and combustion pressure. In the case of the measurements taken, 9 and 8 piston slap events were observed at the TS and ATS respectively. It follows the hypothesis that the higher energy events take place due to piston slap as shown in Fig. 42. Furthermore, it is worth noting that piston slap events present a wide range of frequencies due to the micro asperities which can be assumed as small hammers, that stimulate the structure and the elastic deformations of the competing asperities contribute to the transmittance of noise through the structure [41-43].

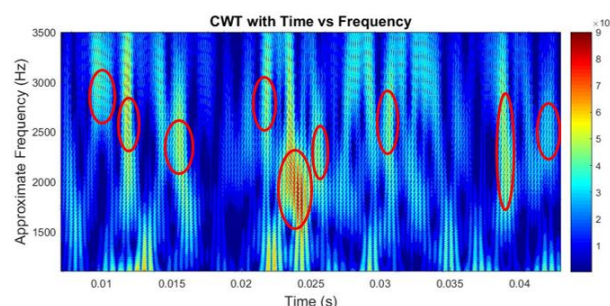


Fig. 42. Recorded piston slap events for position 1 (TDC and TS).

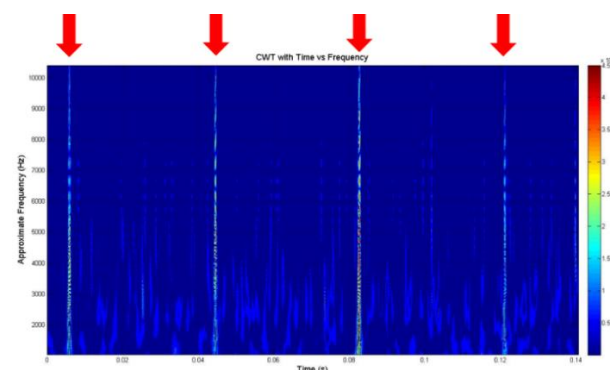


Fig. 43. Frequency - Time diagram of continuous wavelet transform (CWT) for scales [1,10] and step 0.001 for the position 3.

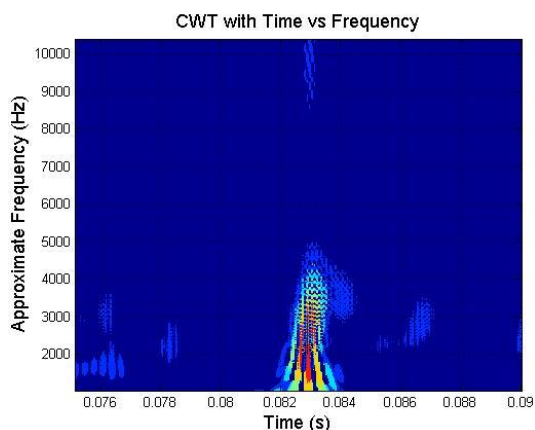


Fig. 44. CWT of the combustion region applying bandpass filter [450-3500Hz] for position 3.

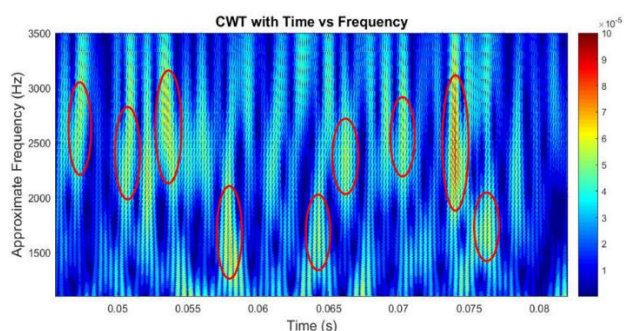


Fig. 45. Recorded piston slap events for position 3 (TDC and ATS).

7.2 Cranckshaft measurements

Beyond the measurements from the TDC, two more set of measurements were conducted at crankshaft in order to identify the effect of the lubrication at crankshaft on the piston slap. The FFT results of the measurements are shown at the Fig. 46.

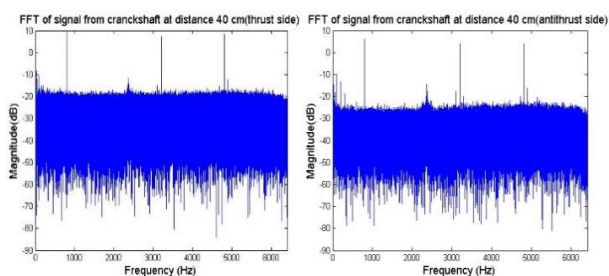


Fig. 46. Absolute value of Fast Fourier Transform (FFT) for the position 2 (left) and 4 (right).

At the moments 0.05 sec and 0.12 sec at TS and ATS respectively the major piston slap events are observed for each case. The other events are shown with the red circles on the figures. Totally, at TS 6 piston slap events were identified and at the ATS 5 piston slap events.

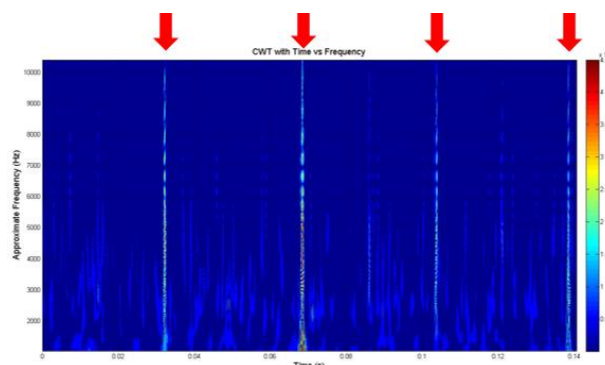


Fig. 47. Frequency - Time diagram of continuous wavelet transform (CWT) for scales [1,10] and step 0.001 for the position 2.

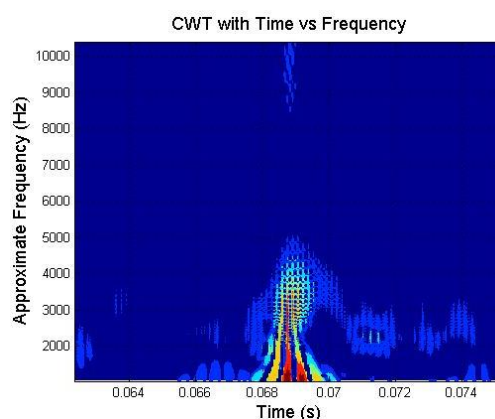


Fig. 48. CWT of the combustion region applying bandpass filter [450-3500Hz] for position 2.

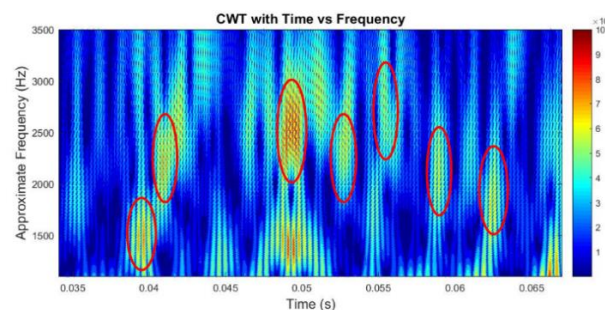


Fig. 49. Recorded piston slap events for position 2 (crankshaft and TS).

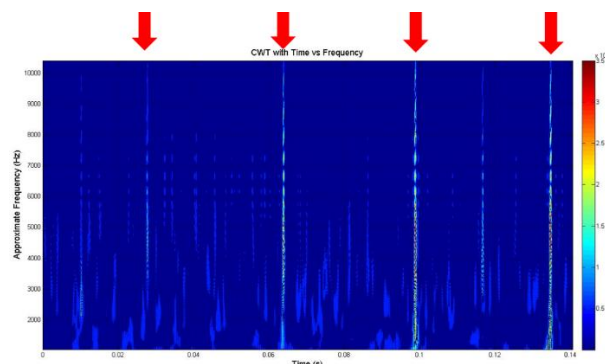


Fig. 50. Frequency - Time diagram of continuous wavelet transform (CWT) for scales [1,10] and step 0.001 for the position 4.

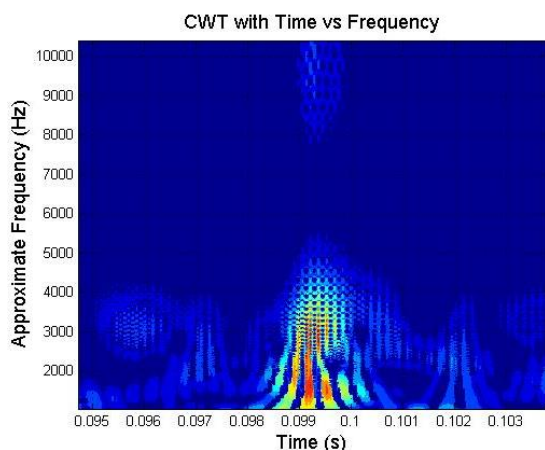


Fig. 51. CWT of the combustion region applying bandpass filter [450-3500Hz] for position 4.

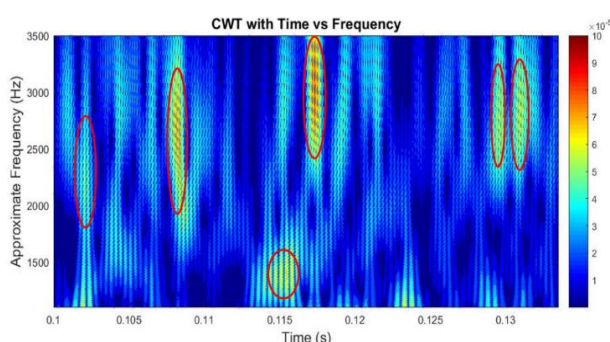


Fig. 52. Recorded piston slap events for position 4 (crankshaft and ATS).

Observing the above figures, it is concluded that there were obviously fewer events than those recorded at the TDC, which is completely reasonable. The similarity between the diagrams for the two aforementioned cases is due to the fact that the distance between the crankshaft axis and the TDC is very small and 6 events were identified. In this set of measurements, piston slap dominated those, corresponding to the TDC and BDC where lubrication on the crankshaft bearings became mixed or boundary. It has also been verified that combustion is a super - Gaussian signal while the piston slap sub - Gaussian. The piston slap involving the friction of the compression rings reaches to its maximum value at the combustion stroke because the lubrication of the compression ring passes from hydrodynamic to boundary/mixed which means that asperities may come in contact to each other. Various other sources that could cause deformation and therefore vibration are oil shearing and cavitation of the oil film.

8. CONCLUSIONS

In this paper, the distribution of pressures on the parabolic profile of the upper compression ring was carried out developing a 2D CFD model under isothermal and quasi-static conditions. More specifically, for a crank angle of 365° the maximum hydrodynamic pressure of 8.08MPa was observed and the minimum lubricant thickness was $0.3 \mu\text{m}$ and regarding the other angles the inlet reversal was also observed. In addition to the friction diagram, it has been found that close to the TDC and after the combustion, there is a greater contribution to friction, whereas in other cases the viscous friction due to shearing of the lubricant has a greater contribution. Along with the friction, the sound pressure level (SPL) were also calculated, which is the highest after combustion and is equal to 86 dB. From the acoustic measurements, a satisfactory number of piston slaps were recorded, and more specifically for the TDC 9 in TS and 8 in the ATS and for the crankshaft 6 in TS and ATS. It has also been shown that the piston slap is a phenomenon with a wide range of frequencies due to the micro asperities oscillating at different frequencies. Furthermore, it was found that the largest piston slap is made at the TDC of combustion stroke and smaller at the remaining dead centers.

The main conclusion of this publication is that the developed numerical methodology has the ability to predict the value of the SPL due to friction (piston slap and micro asperities) which if added to the combustion represents satisfactorily the sound identity of an engine and therefore of a vehicle. The developed code can be applied in the design phase of compression rings where the engine rotates at low angular speeds, and is capable of modeling the engine state, when it is cold during the start or in a traffic jam where the vehicle is moving at low speeds too.

Acknowledgement

The authors would like to acknowledge, Professor John Sakelariou for his help in the measurements using the device of Fig. 9.

REFERENCES

- [1] A. Ruiz-Padillo, D.P. Ruiz, A.J. Torija, Á. Ramos-Ridao, *Selection of suitable alternatives to reduce the environmental impact of road traffic noise using a fuzzy multi-criteria decision model*, *Environmental Impact Assessment Review*, vol. 61, pp. 8–18, 2016, doi: [10.1016/j.eiar.2016.06.003](https://doi.org/10.1016/j.eiar.2016.06.003)
- [2] X. Zhao, Y. Cheng, L. Wang, S. Ji, *Real time identification of the internal combustion engine combustion parameters based on the vibration velocity signal*, *Journal of Sound and Vibration*, vol. 390, pp. 205–217, 2017, doi: [10.1016/j.jsv.2016.11.013](https://doi.org/10.1016/j.jsv.2016.11.013)
- [3] D. Sachau, S. Jukkert, N. Hövelmann, *Development and experimental verification of a robust active noise control system for a diesel engine in submarines*, *Journal of Sound and Vibration*, vol. 375, pp. 1–18, 2016, doi: [10.1016/j.jsv.2016.04.016](https://doi.org/10.1016/j.jsv.2016.04.016)
- [4] M.E. Badaoui, J. Danière, F. Guillet, C. Servièrè, *Separation of combustion noise and piston-slap in diesel engine - Part I: Separation of combustion noise and piston-slap in diesel engine by cyclic Wiener filtering*, *Mechanical Systems and Signal Processing*, vol. 19, iss. 6, pp. 1209–1217, 2005, doi: [10.1016/j.ymssp.2005.08.010](https://doi.org/10.1016/j.ymssp.2005.08.010)
- [5] C. Servièrè, J.-L. Lacoume, M. El Badaoui, *Separation of combustion noise and piston-slap in diesel engine - Part II: Separation of combustion noise and piston-slap using blind source separation methods*, *Mechanical Systems and Signal Processing*, vol. 19, iss. 6, pp. 1218–1229, 2005, doi: [10.1016/j.ymssp.2005.08.026](https://doi.org/10.1016/j.ymssp.2005.08.026)
- [6] Z.-Y. Hao, Y. Jin, C. Yang, *Study of engine noise based on independent component analysis*, *Journal of Zhejiang University-SCIENCE A*, vol. 8, iss. 5, pp. 772–777, 2007, doi: [10.1631/jzus.2007.A0772](https://doi.org/10.1631/jzus.2007.A0772)
- [7] X. Wang, F. Bi, C. Liu, X. Du, K. Shao, *Blind source separation and identification of internal combustion engine noise based on independent component and wavelet analysis*, in *Proceedings of the 2nd Annual Conference on Electrical and Control Engineering, ICECE 2011*, pp. 113–116, China, September 2011, doi: [10.1109/ICECENG.2011.6057519](https://doi.org/10.1109/ICECENG.2011.6057519)
- [8] L. Pruvost, Q. Leclère, E. Parizet, *Diesel engine combustion and mechanical noise separation using an improved spectrofilter*, *Mechanical Systems and Signal Processing*, vol. 23, iss. 7, pp. 2072–2087, 2009, doi: [10.1016/j.ymssp.2009.04.001](https://doi.org/10.1016/j.ymssp.2009.04.001)
- [9] J. Antoni, N. Ducleaux, G. Nghiem, S. Wang, *Separation of combustion noise in IC engines under cyclo-non-stationary regime*, *Mechanical Systems and Signal Processing*, vol. 38, iss. 1, pp. 223–236, 2013, doi: [10.1016/j.ymssp.2013.02.015](https://doi.org/10.1016/j.ymssp.2013.02.015)
- [10] J. Zhang, J. Wang, J. Lin, F. Bi, Q. Guo, K. Chen, L. Ma, *Diesel engine noise source identification based on EEMD, coherent power spectrum analysis and improved AHP*, *Measurement Science and Technology*, vol. 26, no. 9, 2015, doi: [10.1088/0957-0233/26/9/095010](https://doi.org/10.1088/0957-0233/26/9/095010)
- [11] F. Bi, L. Li, J. Zhang, T. Ma, *Source identification of gasoline engine noise based on continuous wavelet transform and EEMD-RobustICA*, *Applied Acoustics*, vol. 100, pp. 34–42, 2015, doi: [10.1016/j.apacoust.2015.07.007](https://doi.org/10.1016/j.apacoust.2015.07.007)
- [12] J. Seifriedsberger, P. Rimplmayr, *Evaluation of the combustion noise of passenger car diesel engines*, *Automotive and Engine Technology*, vol. 1, iss. 1–4, pp. 47–56, 2016, doi: [10.1007/s41104-016-0001-5](https://doi.org/10.1007/s41104-016-0001-5)
- [13] L. Cohen, *Time-Frequency Distributions—A Review*, *Proc. IEEE*, 77, No. 7, pp. 941–981, 1989.
- [14] L. Atlas, P. Duhamel, *Recent Developments in the Core of Digital Signal Processing*, *IEEE Signal Processing Magazines*, vol. 16, iss. 1, pp. 16–31, 1999, doi: [10.1109/79.743864](https://doi.org/10.1109/79.743864)
- [15] N. Dolatabadi, B. Littlefair, M. Delacruz, S. Theodossiades, S. Rothberg, H. Rahnejat, *A transient tribodynamic approach for the calculation of internal combustion engine piston slap noise*, *Journal of Sound and Vibration*, Vol. 352, pp. 192–209, 2015, doi: [10.1016/j.jsv.2015.04.014](https://doi.org/10.1016/j.jsv.2015.04.014)
- [16] N. Dolatabadi, S. Theodossiades, S.J. Rothberg, *On the identification of piston slap events in internal combustion engines using tribodynamic analysis*, *Journal of Mechanical Systems and Signal Processing*, vol. 58-59, pp. 308–324, 2015, doi: [10.1016/j.ymssp.2014.11.012](https://doi.org/10.1016/j.ymssp.2014.11.012)
- [17] K. Ohta, Y. Irie, K. Yamamoto, H. Ishikawa, *Piston slap induced noise and vibration of internal combustion engines* (1st Report, Theoretical Analysis and Simulation), *SAE Technical Paper* 870990, 1987.
- [18] K. Nakashima, Y. Yajima, K. Suzuki, *Approach to minimization of piston slap force for noise reduction—investigation of piston slap force by numerical simulation*, *JSAE Review*, vol. 20, iss. 2, pp. 211–216, 1999, doi: [10.1016/S0389-4304\(98\)00077-0](https://doi.org/10.1016/S0389-4304(98)00077-0)
- [19] H. Shahmohamadi, R. Rahmani, H. Rahnejat, C.P. Garner, P.D. King, *Thermo-mixed hydrodynamics of Piston Compression Ring Conjunction*, *Tribology Letters*, vol. 51, iss. 3, pp. 323-340, 2013, doi: [10.1007/s11249-013-0163-5](https://doi.org/10.1007/s11249-013-0163-5)
- [20] P.C. Mishra, H. Rahnejat, and P.D. King, *Tribology of the ring-bore conjunction subject to a mixed regime of lubrication*, *Proceedings of the*

- Institution of Mechanical Engineers, Part C: Journal of Mechanical Engineering Science, vol. 223, iss. 4, pp. 987-998, 2009, doi: [10.1243%2F09544062JMES1220](https://doi.org/10.1243/2F09544062JMES1220)
- [21] X. Liu, R.B. Randall, *Blind source separation of internal combustion engine piston slap from other measured vibration signals*, Journal of Mechanical Systems and Signal Processing, vol. 19, iss. 6, pp. 1196-1208, 2005, doi: [10.1016/j.ymsp.2005.08.004](https://doi.org/10.1016/j.ymsp.2005.08.004)
- [22] A. Zavos, P.G. Nikolakopoulos, *Computational fluid dynamics analysis of top compression ring in mixed lubrication*, Mechanics & Industry, vol. 18, no. 2, p. 208, 2017, doi: [10.1051/meca/2016024](https://doi.org/10.1051/meca/2016024)
- [23] P. Andersson, J. Tamminen, C.-E. Sandström, *Piston ring tribology: A literature survey*, Espoo 2002: VTT Tiedotteita – Research Notes 2178, 2002.
- [24] M.A. Ejakov, A.R. Diaz, H.J. Chock, *Numerical optimization of ring-pack behaviour*, Society of Automotive Engineers, SAE Technical Paper, p. 12, 1999, doi: [10.4271/1999-01-1521](https://doi.org/10.4271/1999-01-1521)
- [25] N. Morris, R. Rahmani, H. Rahnejat, P.D. King, B. Fitzsimons, *Tribology of piston compression ring conjunction under transient thermal mixed regime of lubrication*, Tribology International, vol. 59, pp. 248-258, 2013, doi: [10.1016/j.triboint.2012.09.002](https://doi.org/10.1016/j.triboint.2012.09.002)
- [26] P. Kohnke, Theory Reference for the Mechanical APDL and Mechanical Applications, ANSYS Inc, Canonsburg, PA, USA, 2009
- [27] SV 12L ½" Microphone preamplifier, available at: http://en.wikipedia.org/wiki/Fluid_bearing, accessed: 29.07.2019.
- [28] SPECIFICATIONS NI cDAQ™-9188, available at: <http://www.ni.com/pdf/manuals/370086c.pdf>, accessed: 29.07.2019.
- [29] E.E. Ungar, D. Ross, *Vibrations and noise due to piston-slap in reciprocating machinery*, Journal of Sound and Vibration, vol. 2, iss. 2, pp. 132-146, 1965, doi: [10.1016/0022-460X\(65\)90091-X](https://doi.org/10.1016/0022-460X(65)90091-X)
- [30] F. Fahy, P. Gardonio, *Sound and Structural Vibration: Radiation, Transmission and Response*, Netherlands: Academic Press, 2007.
- [31] C.F. Ansley, *Computation of the theoretical autocovariance function for a vector arma process*, Journal of Statistical Computation and Simulation, vol. 12, iss. 1, pp. 15-24, 1980, doi: [10.1080/00949658008810423](https://doi.org/10.1080/00949658008810423)
- [32] P.J. Brockwell, R.A. Davis, *Introduction to Time Series and Forecasting*, Second Edition. New York: Springer, 2001.
- [33] A. Zavos, P.G. Nikolakopoulos, *Tribology of new thin compression ring of fired engine under controlled conditions—A combined experimental and numerical study*, Tribology International, vol. 128, pp. 214-230, 2018, doi: [10.1016/j.triboint.2018.07.034](https://doi.org/10.1016/j.triboint.2018.07.034)
- [34] H. Mahdisoozani, M. Mohsenizadeh, M. Bahiraei, A. Kasaeian, A. Daneshvar, M. Goodarzi, M. Reza Safaei, *Performance Enhancement of Internal Combustion Engines through Vibration Control: State of the Art and Challenges*, Applied Science, vol. 9, iss. 3, p. 406, 2019, doi: [10.3390/app9030406](https://doi.org/10.3390/app9030406)
- [35] B. Rahmaniane, M. Reza Safaeia, S.N. Kazia, G. Ahmadib, H.F.Oztopc, K. Vafaid, *Investigation of pollutant reduction by simulation of turbulent non-premixed pulverized coal combustion*, Applied Thermal Engineering, vol. 73, iss. 1, pp. 1222-1235, 2014, doi: [10.1016/j.applthermaleng.2014.09.016](https://doi.org/10.1016/j.applthermaleng.2014.09.016)
- [36] E. Sadeghinezhada, S.N. Kazia, F. Sadeghinejadb, A. Badarudina, M. Mehralic, R. Sadria, M. Reza Safaei, *A comprehensive literature review of bio-fuel performance in internal combustion engine and relevant costs involvement*, Renewable and Sustainable Energy Reviews, vol. 30, pp. 29-44, 2014, doi: [10.1016/j.rser.2013.09.022](https://doi.org/10.1016/j.rser.2013.09.022)
- [37] G. Stachowiak, A. Batchelor, *Engineering Tribology. 3rd Edition*. Oxford (UK): Butterworth-Heinemann, 2006.
- [38] B.-H. Rho, D.-G. Kim, K.-W. Kim, *Noise analysis of oil-lubricated journal bearings*, Proceedings of the Institution of Mechanical Engineers Part C: Journal of Mechanical Engineering Science, vol. 217, iss. 3, pp. 365-371, 2003, doi: [10.1243%2F095440603762870027](https://doi.org/10.1243/2F095440603762870027)
- [39] L. Ver Istvan, L. L. Beranek, *Noise and Vibration Control Engineering: Principles and Applications, 2nd Edition*. John Wiley & Sons Inc, 2006.
- [40] P. Addison, *The illustrated Wavelet Transform Handbook*. Bristol and Philadelphia: Institute of Physics Publishing, 2002.
- [41] A. Le Bot, *Noise of sliding rough contact*, Journal of Physics: Conference Series, vol. 797, 2017, doi: [10.1088/1742-6596/797/1/012006](https://doi.org/10.1088/1742-6596/797/1/012006)
- [42] B.L. Stoimenov, S. Maruyama, K. Adachi, K. Kato, *The roughness effect on the frequency of frictional sound*, Tribology International, vol. 40, iss. 4, pp. 659-664, 2007, doi: [10.1016/j.triboint.2005.11.010](https://doi.org/10.1016/j.triboint.2005.11.010)
- [43] H.B. Abdelounis, A. Le Bot, J. Perret-Liaudet, H. Zahouani, *An experimental study on roughness noise of dry rough flat surfaces*, Wear, vol. 268, iss. 1-2, pp. 335-345, 2010, doi: [10.1016/j.wear.2009.08.024](https://doi.org/10.1016/j.wear.2009.08.024)